



## RESEARCH ARTICLE

10.1029/2022SW003312

### Key Points:

- Quasi 2-dimensional snapshots of nighttime mid-latitude topside perturbations are taken by Swarm satellites in tandem
- The perturbation directions conform to the backward-C shape straddling the dip equator, which is a well-known characteristic of medium-scale traveling ionospheric disturbances
- The in-situ perturbations can also disturb topside total electron content above Swarm

### Supporting Information:

Supporting Information may be found in the online version of this article.

### Correspondence to:

H. Song,  
[hssong@kasi.re.kr](mailto:hssong@kasi.re.kr)

### Citation:

Song, H., Park, J., Jin, Y., Otsuka, Y., Buchert, S., Lee, J., & Yi, Y. (2023). Tandem observations of nighttime mid-latitude topside ionospheric perturbations. *Space Weather*, 21, e2022SW003312. <https://doi.org/10.1029/2022SW003312>

Received 5 OCT 2022

Accepted 26 JAN 2023

### Author Contributions:

**Conceptualization:** Hosub Song, Jaeheung Park

**Formal analysis:** Hosub Song, Yaqi Jin, Yuichi Otsuka, Stephan Buchert

**Investigation:** Hosub Song, Yaqi Jin, Stephan Buchert

**Methodology:** Hosub Song, Jaeheung Park

**Project Administration:** Jaeheung Park

**Resources:** Hosub Song

**Software:** Hosub Song

**Supervision:** Jaejin Lee, Yu Yi

# Tandem Observations of Nighttime Mid-Latitude Topside Ionospheric Perturbations

Hosub Song<sup>1,2</sup> , Jaeheung Park<sup>1,3</sup> , Yaqi Jin<sup>4</sup> , Yuichi Otsuka<sup>5</sup> , Stephan Buchert<sup>6</sup> , Jaejin Lee<sup>1</sup> , and Yu Yi<sup>2</sup> 

<sup>1</sup>Space Science Division, Korea Astronomy and Space Science Institute (KASI), Daejeon, South Korea, <sup>2</sup>Department of Astronomy, Space Science and Geology, Chungnam National University (CNU), Daejeon, South Korea, <sup>3</sup>Department of Astronomy and Space Science, University of Science and Technology (UST), Daejeon, South Korea, <sup>4</sup>Department of Physics, University of Oslo, Oslo, Norway, <sup>5</sup>Institute for Space-Earth Environmental Research, Nagoya University, Nagoya, Japan, <sup>6</sup>Swedish Institute of Space Physics, Uppsala, Sweden

**Abstract** Nighttime medium-scale traveling ionospheric disturbances (MSTIDs) have been generally observed by ground-based instruments. However, they provide 2-dimensional images over only a limited field of view and are not distributed globally. The ground-based observations reported that MSTID wavefronts exhibit backward-C shapes virtually straddling the dip equator. In situ plasma density measurements onboard individual satellites could overcome the limited coverage of ground-based MSTID observations. But, most of those spacecrafts could obtain only 1-dimensional profiles of plasma density, which leaves uncertain whether the observed perturbations generally have the characteristic directivity of MSTIDs. This paper addresses this knowledge gap by statistically investigating nighttime perturbations in the mid-latitude topside ionosphere observed by tandem satellites, Swarm A and C. We cross-correlate the plasma density profiles observed by Swarm A and C. The correlation coefficient tends to increase as the two spacecraft move closer, allowing us to derive the disturbances' directivity whenever the Swarm A and C observations are correlated significantly. The directivity statistics agree well with the backward-C shape. Furthermore, the wavefront directions have clear dependence on magnetic latitudes while they are not as well aligned with local time, which is also consistent with previous reports on nighttime MSTIDs using ground-based observations and computer simulations. Additionally, we demonstrate that the nighttime MSTIDs can increase the topside Rate Of Total electron content Index above Swarm. All the above-mentioned results support that the nighttime mid-latitude perturbations observed by Swarm can be identified as MSTIDs on the whole, which is the most important finding of this paper.

**Plain Language Summary** In this paper, we statistically study the characteristics of nighttime plasma perturbations in the mid-latitude topside using Swarm satellites. Conventionally, observations of those midlatitude perturbations heavily relied on ground-based facilities, such as global positioning system (GPS) receivers, All-Sky Cameras, and radars, from which we can obtain 2-dimensional (2D) images of the medium-scale traveling ionospheric disturbances (MSTIDs). On the other hand, in situ plasma density measured onboard individual Low Earth Orbit (LEO) satellites, which can cover the whole globe, only provided 1-dimensional (1D) profiles, making it difficult to investigate the 2D morphology of perturbations. With two satellites flying side by side, we can overcome the limitation of the LEO in situ observations, which is the topic of this study. The results show that the 2D morphology of the perturbations in the nighttime mid-latitude topside ionosphere agrees with the known properties of MSTIDs reported in previous ground-based studies: backward-C shape virtually straddling the dip equator. We also demonstrate that the MSTIDs can perturb the total electron content above Swarm, which supports that MSTIDs can exist even above Swarm heights and that they can disturb radio communication between Swarm and GPS satellites.

## 1. Introduction

Traveling ionospheric disturbance (TID) represents horizontally propagating wave-like electron density disturbance (Frissell et al., 2022; Kil & Paxton., 2017; Otsuka et al., 2004; Shiokawa et al., 2003; Tsugawa et al., 2007). TID is generally classified into large-scale TID (LSTID) and medium-scale TID (MSTID) (Hernández et al., 2011). The LSTIDs have a period of >1 hr, move faster than 400 m/s, and have a horizontal wavelength of >1,000 km (Hunsucker, 1982). The main driver of LSTID is believed to be Joule heating, which results from

© 2023. The Authors.

This is an open access article under the terms of the [Creative Commons Attribution-NonCommercial-NoDerivs License](https://creativecommons.org/licenses/by-nc-nd/4.0/), which permits use and distribution in any medium, provided the original work is properly cited, the use is non-commercial and no modifications or adaptations are made.

**Validation:** Hosub Song, Jaeheung Park, Yaqi Jin, Yuichi Otsuka, Stephan Buchert, Jaemin Lee, Yu Yi

**Visualization:** Hosub Song

**Writing – original draft:** Hosub Song

**Writing – review & editing:** Jaeheung Park, Yaqi Jin, Yuichi Otsuka, Stephan Buchert, Jaemin Lee, Yu Yi

the energy flowing from the magnetosphere to the auroral ionosphere, and particle precipitation during the auroral substorm (Crowley et al., 1987; Hajkowicz, 1990; Hajkowicz & Hunsucker, 1987; Song et al., 2013). On the other hand, MSTID can have horizontal speeds between 50 and 250 m/s, a period between 15 min and 1 hr, and horizontal wavelengths of several hundred km (Hunsucker, 1982; Ogawa et al., 1987). MSTIDs are again classified into day-time MSTIDs heading south or southeast in the Northern Hemisphere (NH) and nighttime MSTIDs propagating southwestward in the NH, meaning that their generation mechanisms are different (Sivakandan et al., 2021; Tsugawa et al., 2007). Specifically, the wavefront directions of nighttime MSTIDs are known to conform to backward-C shapes virtually straddling the dip equator (e.g., Otsuka et al., 2004). The causes of nighttime MSTID are dominantly attributed to electrodynamic mechanisms such as Perkins instability and its synergy with sporadic-E (Es) layers (Otsuka et al., 2007; Park et al., 2010; Saito et al., 2008; Tsunoda, 2006), and day-time MSTID is related to atmospheric gravitational waves (AGWs; MacDougall et al., 2009; Jonah et al., 2017).

Traditionally, TIDs have been studied with different types of ground observation equipment. One of the well-known methods of identifying TID is from the Total Electron Content (TEC) observations using networks of global positioning system (GPS) receivers (Dinsmore et al., 2021; Otsuka et al., 2013; Tsugawa et al., 2007; Zakharenkova et al., 2016). Saito et al. (1998) observed MSTID over Japan for the first time through TEC 2D mapping, and then Perwitasari et al. (2022) analyzed MSTID with 3-Dimensional information from GPS-TEC perturbation. However, in the case of ground-based TEC measurements using GNSS signals, including GPS, it is not easy to observe MSTIDs in remote areas such as the oceans, deserts, and polar regions because the terrain where the receiver is to be installed is lacking (Yang et al., 2021). Several techniques have been developed to estimate the Vertical Total Electron Content (VTEC) in areas without GNSS receivers (Jeong et al., 2022; Nematipour et al., 2022; Scharroo & Smith, 2010). However, these estimation techniques are generally unsuitable for investigating ionospheric irregularities, such as MSTID. All-sky imagers, which use high-sensitivity cooling CCD cameras, also observed 2D images in a 630.0 nm red visible wavelength (Mendillo et al., 1997; Otsuka et al., 2012). Other conventional methods of observing TIDs include High-Frequency Doppler radars (Frissell et al., 2016), incoherent scatter radars (Zhang et al., 2021), and ionosondes (Altadill et al., 2020).

The limited spatial coverage of ground-based instruments can be overcome by satellites that monitor the entire globe (e.g., Su et al., 2006). Several studies reported statistical distributions of nighttime mid-latitude perturbations or undulations observed in situ and attributed them to MSTIDs. However, most of them were based on 1-dimensional (1D) plasma density profiles along individual satellite tracks (Lee et al., 2021; Park et al., 2010), except for a few case studies (e.g., Kil et al., 2019). As a result, it is not 100% certain whether those in situ disturbances climatologically exhibit characteristic properties of MSTIDs, such as the above-mentioned directivity of wave propagation or wavefronts (i.e., the backward-C shape). To the best of the authors' knowledge, only Rajesh et al. (2016) statistically investigated full 2D images of MSTIDs taken onboard a spacecraft, FORMOSAT-2/ISUAL although the amount of analyzed data was small. As ground observation and satellite measurement have their advantages and disadvantages (e.g., limited coverage of ground-based observation and general lack of 2D view from in situ measurements), various data were analyzed together in some case studies to effectively deduce the characteristics of MSTID (Ogawa et al., 2009; Onishi et al., 2009).

While there have been statistical MSTID studies through satellite-based observations, the 1D data cannot provide key information (e.g., the wavefront directivity) about MSTIDs. Also, the coherence length scale of MSTIDs, at which two latitudinal cross sections of the wavefronts lose coherence, is not quantitatively addressed yet. Though several case studies at individual regions (e.g., Yadav et al., 2021) reported the finiteness of MSTID wavefronts, no global-scale statistics have been compiled for this topic. Therefore, MSTIDs were often assumed to be infinite plane waves in simplified schematics (e.g., Ogawa et al., 2009, Figure 13). In addition, MSTID effects on topside TEC have not been statistically investigated while there have been studies using ground-based TEC and satellite-based in situ plasma density.

In this paper, we first deduce quasi-2D images of nighttime mid-latitude topside perturbations using plasma density data of Swarm A and C satellites. Unlike ground-based imagers, this quasi-2D analysis using tandem satellite measurements can cover the entire world, including areas such as deserts and oceans where GPS receivers are not located. Second, we demonstrate that the MSTIDs are not infinite plane waves, but can exhibit inhomogeneity or finiteness along the wavefront. Third, we analyze the Rate Of TEC Index (ROTI) data around MSTIDs, which represent disturbance levels of topside TECs above Swarm satellites.

In Section 2, the methodology is introduced. Swarm A and C satellites measure electron density in tandem at adjacent longitudes. By cross-correlating the two spacecraft data, we can derive the wavefront direction of perturbations. Section 3 first presents the seasonal and geographical distribution of our events, which agrees with previous studies on MSTIDs. The directivity of perturbations obtained from the cross-correlation method will be shown for different latitudes or local time ranges. In addition, we also demonstrate the association of the in-situ disturbances with the ROTI above Swarm. In Section 4, we discuss the topside nighttime mid-latitude perturbations in the context of previous studies on MSTIDs. Finally, Section 5 summarizes the main (observations) findings.

## 2. Swarm Satellites and Data Processing Methods

### 2.1. Swarm Satellites

The Swarm mission consists of a group of three satellites, launched on 22 November 2013 and operated by the European Space Agency (ESA) (Park et al., 2015). These satellites have polar orbits with an inclination angle of about  $88^\circ$  (Friis-Christensen et al., 2008). The altitude of Swarm A and C is  $\sim 460$  km, and the altitude of Swarm-B is 500 km with a slightly different inclination angle from those of the two other spacecraft (Knudsen et al., 2017). While Swarm A and C are at the same altitude, they were maintained for many years at a zonal separation of about  $1.4^\circ$  in geographic longitude (GLON), and the zonal distance has been changed only recently (Lühr et al., 2019; Park, 2022).

Swarm satellites are equipped with an Electric Field Instrument (EFI) consisting of two Thermal Ion Imagers (TIIs) and two Langmuir Probes (LPs) (Buchert et al., 2015; Knudsen et al., 2017). LPs are equipment to measure electron temperature and density in-situ (Song, Park, et al., 2022; Yin et al., 2019). LPs apply a voltage (bias) to the exposed collector surface and measure the current (Oyama, 2015; Smirnov et al., 2021). The temperature ( $T_e$ ) and density ( $N_e$ ) of electrons can be derived from the Langmuir probe observations (Ryu et al., 2017). A negative bias is applied for estimating the density with the Swarm LPs, and the ion current is measured. Since the ionospheric plasma is quasi-neutral, we assume that  $N_i = N_e$ . In this study we use 1 Hz  $N_e$  data from the Ionospheric Plasma IRregularities (IPIR) product from 16 July 2014, to 16 February 2022 (e.g., Jin et al., 2022).

Another payload carried by Swarm satellites is GPS Receivers (GPSR; Zakharenkova et al., 2019). The GPSR has eight channels that simultaneously receive signals from several GPS satellites. Also, this instrument analyzes the phase differences between GPS signals to derive the Total Electron Content (TEC), which means the number of electrons between GPS satellites and Swarm per unit cross-section. The vertical TEC, where the obliquity factor of the Line-Of-Sight (LOS) between the GPS and Swarm satellites is considered, is included in the Swarm IPIR product at the same 1 Hz rate as for  $N_e$ .

### 2.2. Data Processing Methods

The wavefront of the nighttime MSTID is known to be tilted with respect to the magnetic meridian (e.g., Otsuka et al., 2004), which conforms to the backward-C shape virtually straddling the dip equator. Thanks to the formation flight of Swarm A and C, we can investigate whether the topside disturbances observed by Swarm exhibit similar directivity. To derive the angle between the magnetic meridian and wavefront directions, we first search for similar patterns in electron density profiles observed by Swarm A and C, based on the cross-correlation coefficient. If the two similar patterns (one for Swarm A and the other for Swarm C) are latitudinally offset from each other, the latitudinal offset combined with the GLON difference between the two spacecraft allows us to deduce the wavefront direction of the observed perturbations: see also Xiong et al. (2016). This is the basic strategy that will be used in the following procedure.

To focus on nighttime mid-latitude  $N_e$  profiles, we crop nighttime Swarm A and C data at mid-latitudes, that is, between  $+20^\circ \sim +55^\circ$  and  $-20^\circ \sim -55^\circ$  of Magnetic LATitude (MLAT) and from Magnetic Local Time (MLT) 19:00 via midnight to 05:00. Each hemispheric segment of the  $N_e$  time series resulting from the above-mentioned cropping (e.g., a short hemispheric piece of  $N_e$  time-series between  $+20$  and  $+55^\circ$  in MLAT) is called “orbit segment” or “event” hereafter. Four segments are in one full orbit: the northern and southern hemispheric segments around the acceding and descending nodes. Among the four, two segments on the nightside are used for further analyses.

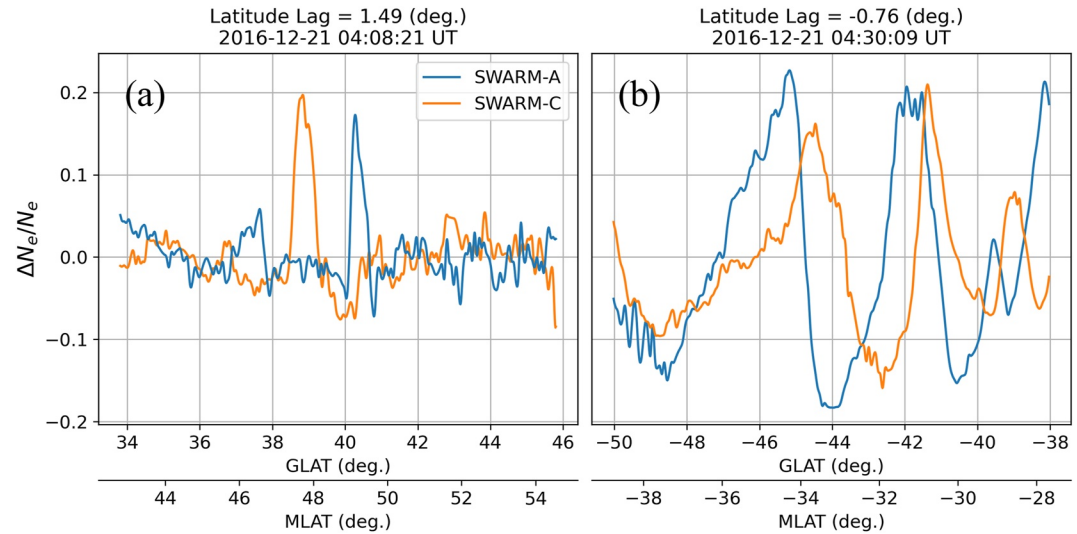


**Figure 1.** Relative electron density perturbation ( $\Delta N_e/N_e^{\text{background}}$ ) of Swarm A and C. The y-axis is the ratio of the electron density variation to the background ( $\Delta N_e/N_e^{\text{background}}$ ), and panels (a and b) share the same y-axis scale. The x-axis represents the Geographical LATitude (GLAT) and Magnetic LATitude (MLAT). Panels (a and 1) correspond to the northern and southern hemispheres respectively, as can be seen in the different signs of GLAT. The blue solid line represents Swarm-A, and the orange solid line is data measured by Swarm-C. The latitude offset (or latitude lag) between Swarm A and C is 1.49° in (a) and −0.76° in (b), as shown in the title of each panel. If we combine the latitude offset with the difference in longitude between Swarm A and C, we can deduce the wavefront directions of the perturbations observed by Swarm A and C.

To cross-correlate the Ne data of Swarm A and C, we interpolate them at 0.01° Geographic LATitude (GLAT) intervals through the *interpolate* function of the Python SciPy package. Then, two Savitzky-Golay filters (*savgol\_filter* function of Python SciPy) with different window sizes are simultaneously applied to each orbit segment to extract the band-pass-filtered signal of Ne. As MLAT of 20° ~ 55° (spanning 35° in MLAT) is used, the total number of data points per segment is approximately 3,500 ( $=35^\circ \div 0.01^\circ$  resolution). After some experiments with window sizes of the Savitzky-Golay filter, we have finally set the outer window length to 1,300 ( $=13^\circ$  GLAT range  $\div 0.01^\circ$  resolution) and the inner window length to 13 ( $=0.13^\circ$  GLAT range  $\div 0.01^\circ$  resolution). The purpose of the outer window length is to remove the background large-scale trend, and that of the inner window length is to reduce small-scale noise.  $\Delta N_e$  is the residual obtained by subtracting the outer-window result from the inner-window one, which can be considered as a band-pass-filtered signal of Ne. Dividing  $\Delta N_e$  again by the outer-window data ( $N_e^{\text{background}}$ ) results in  $\Delta N_e/N_e^{\text{background}}$ , which represents relative fluctuation levels of Ne and will be used as a key parameter in the following analyses.

Next, we find up to 5 largest peaks of  $|\Delta N_e|$  in each orbit segment in the Swarm-C data. This criterion allows us to focus on strong plasma perturbations and prevents contamination from weak non-geophysical noises sitting on smooth background profiles. For each of the five peaks, cross-correlation coefficients and lags between Swarm A and C data ( $\Delta N_e/N_e^{\text{background}}$ ) are calculated within  $\pm 6$  degrees of GLAT around each peak. As a result, we obtain 5 cross-correlation coefficients ( $R$ ) and lags per orbit segment. The largest  $R$  among the five correlation coefficients is named  $R_{\text{max}}$ , and the corresponding lag is called  $\Delta \text{GLAT}$ . In other words, the  $\Delta N_e/N_e^{\text{background}}$  profiles of Swarm A and C resemble each other best when we shift Swarm-C data by  $\Delta \text{GLAT}$ . Additionally, the standard deviation of  $\Delta N_e/N_e^{\text{background}}$  ( $\Delta N_e$ ) within the very  $\pm 6^\circ$  of GLAT around the  $R_{\text{max}}$  location is recorded as a proxy for relative (absolute) perturbation strength. Note that the latitude range used to calculate  $R_{\text{max}}$  ( $\pm 6^\circ$  or in total  $12^\circ$ ) is already a significant portion (roughly a third) of one pass (MLAT of 20°~55° or in total 35°). Though we select  $R_{\text{max}}$  among five correlation coefficients, it does not mean that  $R_{\text{max}}$  is representative of only 20% of the pass. Rather, each  $R_{\text{max}}$  can largely characterize the pass it belongs to because of the wide GLAT range used for it. We will come back to this issue in Section 4.1.

Figure 1 presents the relative electron density perturbation ( $\Delta N_e/N_e^{\text{background}}$ ) of a representative mid-latitude event as a function of GLAT and MLAT for Swarm A and C, respectively. Figure 1a shows the  $\Delta N_e/N_e^{\text{background}}$  near +40° GLAT at around 04:08:21 on 21 December 2016, in Universal Time (UT), and Figure 1b shows the  $\Delta N_e/N_e^{\text{background}}$  around −60° GLAT which was taken after 20 min. That is, these two graphs are on the same orbit



while Figure 1a is for the northern hemisphere and Figure 1b is for the southern hemisphere. Swarm A (blue) and C (orange) observed similar profiles of plasma density, but the two profiles have a latitudinal offset ( $\Delta\text{GLAT}$  or lag). We determine the exact latitude difference ( $\Delta\text{GLAT}$ ) using the cross-correlation function as mentioned above, which is also shown in the title of each panel in Figure 1 (“Latitude Lag”). Also, the two satellites have different (by  $\sim 1.4^\circ$ ) Geographic LONGitudes (GLON): the offset is denoted  $\Delta\text{GLON}$  hereafter. From the latitudinal and longitudinal offsets, we can deduce the wavefront directions of the electron density disturbance and check whether they conform to the conventionally known directivity of MSTID phase fronts. Specifically, using the spherical trigonometry function of the PyGeodesy python package (`pygeodesy.sphericalTrigonometry.triangle7`) we derive the tilt angle of the wavefront from the geographic north, that is, the geographic tilt angle ( $\theta_{\text{geo}}$ ): positive eastward. The tilt angle from the magnetic north ( $\theta_{\text{mag}}$ ) is derived by correcting  $\theta_{\text{geo}}$  for the magnetic declination (obtained from Chaosmagpy of Python packages). For example,  $\theta_{\text{mag}} = -45^\circ$  ( $+45^\circ$ ) means that the wavefronts of perturbation observed by Swarm A and C are aligned in the magnetically NorthWest-SouthEast (NorthEast-SouthWest) direction. The statistical distributions of  $\theta_{\text{mag}}$  will be addressed in the following Sections.

The method of this study is based on a principle that is similar to those used in analyzing ground-based multi-point measurements (e.g., Huang et al., 2018; Oinats et al., 2016). One important difference is that ground-based techniques can monitor a region for a long time, from which MSTID velocity can be estimated. On the contrary, Low-Earth-Orbit (LEO) spacecraft, such as Swarm used here, moves with a speed ( $\sim 7.5$  km/s) much faster than usual MSTIDs (order of 0.1 km/s) and only provides a snapshot of an MSTID. As a single LEO spacecraft cannot track the temporal evolution of MSTIDs, the data cannot be used to derive MSTID velocity. If we need to derive the MSTID velocity using LEO satellites, we should place multiple spacecraft into a pearls-on-a-string configuration, which may be realized in future missions.

### 3. Result

We first plot the seasonal/geographical distribution of the perturbation events, which will be statistically analyzed in this section, on the world map in Figure 2. The events are chosen based on the following conditions: (a)  $R_{\text{max}} > 0.5$  (to focus on the events where Swarm A and C observed very similar profiles), and (b) the standard deviation of  $\Delta\text{Ne} > 8,000 \text{ cm}^{-3}$  (to avoid smooth Ne profiles without plasma perturbations or contamination from weak non-geophysical noise sitting on them). We have selected the threshold for  $\Delta\text{Ne} (> 8,000 \text{ cm}^{-3})$  considering previous studies on ionospheric irregularities, such as Huang et al. (2014) who used  $> 10,000 \text{ cm}^{-3}$ . Figure 2 presents the locations where  $R_{\text{max}}$  is obtained in each selected orbit segment. The x-axis represents GLON, the y-axis corresponds to GLAT, and the color bar indicates the number of events within a bin. In addition, each panel represents a season: (a) combined equinoxes (March, April, September, and October), (b) June solstice (May–August), and (c) December solstice (November, December, January, and February).

The distribution is very similar to the results of previous LEO-based studies that reported nighttime mid-latitude perturbation distributions using 1D in situ observations (e.g., Lee et al., 2021; Park et al., 2010). The consistency supports that the perturbations events investigated in this paper are similar to what the previous 1D in situ observations addressed and attributed to MSTIDs. The events shown in Figure 2 will be used in the following analyses.

We go a step forward from previous studies by statistically analyzing quasi-2D structures of the observed disturbances. As a first step, in Figure 3, we present the  $R_{\text{max}}$  as a function of  $|\Delta\text{GLON}|$  between the spacecraft. The data period used in this paper, including Figure 3, is from 16 July 2014, to 16 February 2022. Among the selection criteria used for Figure 2, the one criterion,  $R_{\text{max}} > 0.5$  (black dashed line), is relieved in Figure 3, to show that the selected events in Figure 2 constitute the majority of the perturbation events (satisfying the standard deviation of  $\Delta\text{Ne} > 8,000 \text{ cm}^{-3}$ ). The graph on the top row is for the Northern Hemisphere, and the figure below refers to the Southern Hemisphere. The X-axis is the absolute value of the GLON difference between spacecraft ( $|\Delta\text{GLON}|$ ), and the Y-axis is  $R_{\text{max}}$ , which is the maximum cross-correlation coefficient that was obtained by the procedure described in Section 2.2. The solid red line is the mean and the standard deviation of  $R_{\text{max}}$  at regular intervals of  $0.2^\circ |\Delta\text{GLON}|$ , and the color palette used for each pixel in the background signifies the number of events. Swarm satellites operate at  $|\Delta\text{GLON}|$  of about  $1.4^\circ$  for a large part of their lifetime, so most of the events are concentrated at  $|\Delta\text{GLON}| \sim 1.4^\circ$  on the x-axis. When  $|\Delta\text{GLON}|$  is close to zero, nearly the same density profiles should be observed, and the correlation coefficient ( $R_{\text{max}}$ ) is close to 1: that is, the two spacecraft's data sets are nearly redundant. As  $|\Delta\text{GLON}|$  increases, the correlation coefficient also decreases, but even if it is  $1.4^\circ$  away, the maximum correlation coefficient ( $R_{\text{max}}$ ) we obtained remains at 0.6 on average.

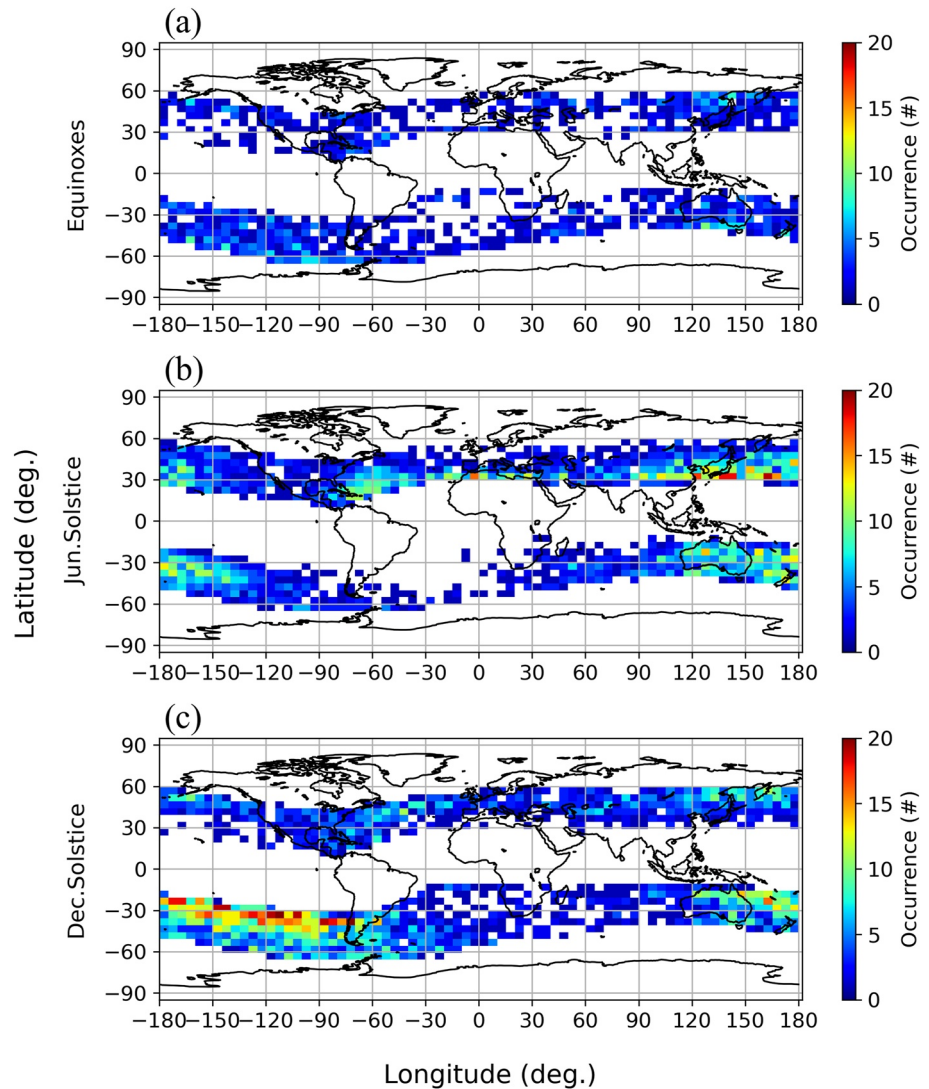


**Figure 2.** Color histograms for the events that will be used in this section. The x-axis is geographical longitude, the y-axis is geographical latitude, and all panels have the same scale axes. Panel (a) shows the number of events during the March and September equinoxes (March, April, September, and October), Panel (b) is during the June solstice (May–August), and Panel (c) corresponds to the December solstice (November, December, January, and February). The colored bins appear only in the range of  $\pm 20$  to  $\pm 55$  degrees of the magnetic latitude used in the analysis. The color bar displays the number of events within each bin.

When the two density profiles of Swarm A and C exhibit high correlation ( $R_{\max} > 0.5$ ), we can reliably deduce the wavefront directions (or directivity) based on the  $\Delta\text{GLAT}$  (or latitude lag) that corresponds to the  $R_{\max}$ . In the northern hemisphere (Figure 3, top panel), out of 4,367 total events of the strong-fluctuation ( $\Delta N_e > 8,000 \text{ cm}^{-3}$ ), just 1,035 events have  $R_{\max}$  less than 0.5, accounting for a minority of 23.7%. Similarly, in the southern hemisphere (Figure 3, bottom panel) only 18.3% of the total 5,659 events have  $R_{\max}$  less than 0.5. In the following, we focus our analyses on those high-correlation ( $R_{\max} > 0.5$ ) events that constitute the majority.

Figure 4 presents the wavefront angle with respect to the geomagnetic north ( $\theta_{\text{mag}}$ ; positive eastward), clockwise when looked at from above. Orange histograms on the top correspond to the Northern Hemisphere, and blue histograms on the bottom represent the Southern Hemisphere. Each row from the left represents an MLAT range:  $|\text{MLAT}|$  increases (i.e., the observation points move from the equator toward the poles) from left to right. Each column spans an MLAT range of  $10^\circ$ : from  $|\text{MLAT}| = 20^\circ$  to  $|\text{MLAT}| = 60^\circ$ . In a semicircular histogram, the length of the bar is the number of events, and the angle of the bar is the angle of the wavefront relative to the magnetic north pole ( $\theta_{\text{mag}}$ ). The median and the Standard Error of the Mean (SEM) of  $\theta_{\text{mag}}$  are annotated below

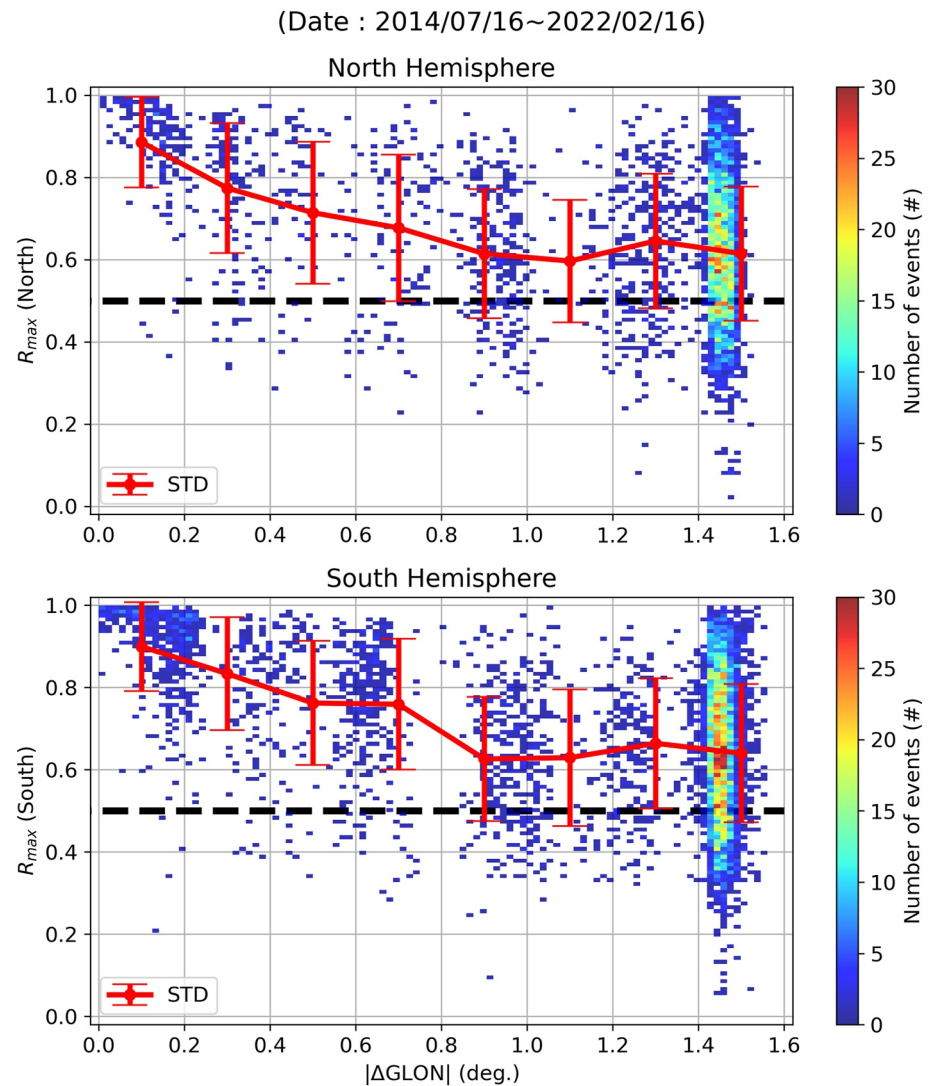


**Figure 3.** Color histogram as a function of the maximum correlation coefficient ( $R_{\max}$ ) obtained between Swarm A and C (y-axis) and the zonal distance between the two spacecraft (x-axis). The x-axis is an absolute value of the GLON difference ( $|\Delta\text{GLON}|$ ) between Swarm A and C at the time of observation. The y-axis is the maximum value of the correlation coefficient obtainable from the Ne profiles from the two satellites ( $R_{\max}$ ). The black dashed line represents  $R_{\max}$  of 0.5, and in this paper, we use only events with  $R_{\max}$  greater than 0.5. The color of each pixel represents the number of events, and most of the events have zonal separation of  $\sim 1.4^\circ$  in GLON (i.e.,  $|\Delta\text{GLON}| \sim 1.4^\circ$ ), which results from the operation history of the Swarm mission. The top and bottom panels correspond to the northern and southern hemispheres, respectively, and the solid red lines represent the mean and standard deviation of  $R_{\max}$  given at regular intervals of  $0.2^\circ |\Delta\text{GLON}|$ .

each panel. The wavefronts of our events are generally in the northwest-southeast direction in the Northern Hemisphere:  $\theta_{\text{mag}}$  is negative in most cases. The trend is reversed in the southern hemisphere:  $\theta_{\text{mag}}$  is generally positive. The hemisphere-dependent polarity of  $\theta_{\text{mag}}$  (or backward-C shape) is in good agreement with the well-known directivity of MSTID wavefronts as reported by previous ground-based observations (e.g., Otsuka et al., 2004; Shiokawa et al., 2003). Furthermore, we can see that wavefronts are more and more inclined toward the magnetic east-west direction as  $|\text{MLAT}|$  increases: that is,  $|\theta_{\text{mag}}|$  increases with  $|\text{MLAT}|$ , as can be seen from the mean  $\theta_{\text{mag}}$  shown below each panel. Interestingly, the absolute values of  $\theta_{\text{mag}}$  are overall larger in the Northern Hemisphere than in the Southern Hemisphere. Similar hemispheric asymmetry in the absolute tilt angles was reported previously for nighttime MSTIDs observed by European and South African ASIs (Martinis et al., 2019).

Figure 5 shows that in situ disturbances are accompanied by fluctuations of topside TEC, which is represented as Rate Of TEC Index (ROTI) data (e.g., Jin et al., 2022). Among the criteria used for Figure 2, the standard

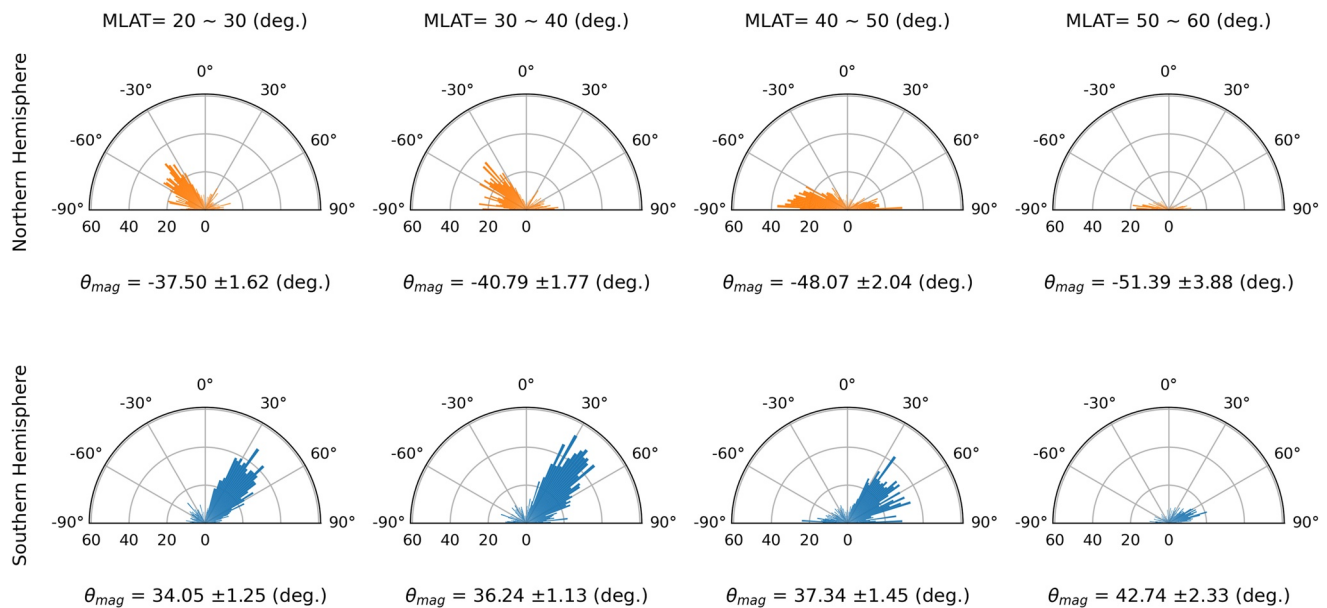


**Figure 4.** Semicircle histograms showing the wavefront direction of the nighttime mid-latitude topside perturbations observed by Swarm A and C. The length of the bars is the number of events, and the angle of the bars represents  $\theta_{mag}$ . The top panels in orange are for the northern hemisphere, and the bottom panels in blue are for the southern hemisphere. The ranges of relevant magnetic latitude (MLAT) are shown on top of the four columns, each  $10^\circ$  wide from  $20^\circ$  to  $60^\circ$  in absolute magnetic latitudes. Below each graph, the median and the Standard Error of the Mean (SEM) of  $\theta_{mag}$  are given. Since the  $\theta_{mag}$  is negative in the northern hemisphere and positive in the southern hemisphere, the Swarm-observed perturbations virtually form backward-C shapes straddling the dip equator.

deviation of  $\Delta Ne > 8,000 \text{ cm}^{-3}$ , is relieved, to incorporate both weak and strong perturbations in the same context. The  $x$ -axis is the standard deviation of the  $\Delta Ne$  within  $\pm 6^\circ$  GLAT around the Rmax position in each of the Swarm-C orbit segments: this value represents the strength of in situ Ne fluctuations. The  $y$ -axis is the median of the mROTI20s data, which means the standard deviation of the rate of TEC over 20 s, in the same GLAT range: this parameter stands for perturbation strength *above* Swarm. The color bar represents the number of events per bin. The upper graphs are for the northern hemisphere, and the lower graphs are for the southern hemisphere. The left column is the June solstice, and the right column is the December solstice. Equinoctial seasons are omitted because of the small number of events, as shown in Figure 2. Figure 5 shows an overall positive relationship between the standard deviation of  $\Delta Ne$  and mROTI20s. In other words, stronger Ne fluctuations at the Swarm position are accompanied by higher mROTI20s or stronger fluctuations of topside TEC above the Swarm. These correlations with topside ROTI indicate that the in situ electron density perturbations observed by Swarm may feature localized electric fields, which are mapped along geomagnetic field lines to connect different altitudes. Note that previous studies (e.g., Otsuka et al., 2004; Shiokawa et al., 2003) similarly associated nighttime MSTIDs with the localized electric field. Hence, Figure 5 supports that the perturbations encountered by Swarm can be identified as nighttime MSTIDs, although we cannot pinpoint the actual source of the electric fields (e.g., from sporadic-E in the same hemisphere to the conjugate E-region through interhemispheric coupling) only with Swarm data. For completeness, we have drawn a plot similar to Figure 5, where we substitute the standard deviation of the  $\Delta Ne$  with that of  $\Delta Ne/Ne_{background}$ . The result (figure not shown) looks qualitatively similar to Figure 5.

## 4. Discussion

### 4.1. Directivity of the Perturbations Observed by Swarm: Evidence for Their Relationship to MSTIDs

As mentioned in Section 1, most previous studies on nighttime mid-latitude topside perturbations (e.g., Park et al., 2010; Su et al., 2006) relied on 1D observations. Some of those studies attributed the perturbations to MSTIDs, but based only on similar seasonal/geographical distributions (Kil & Paxton, 2017; Park et al., 2010) or on a few cases of coordinated (e.g., ground-satellite) observations (e.g., Kil et al., 2019). It is yet to confirm whether the perturbations observed in the nighttime mid-latitude topside are MSTIDs in general. In this context, the wavefront directivity in Figure 4 provides convincing evidence that the nighttime mid-latitude perturbations observed by Swarm, at least the events that can leave strong and coherent signatures on both Swarm A



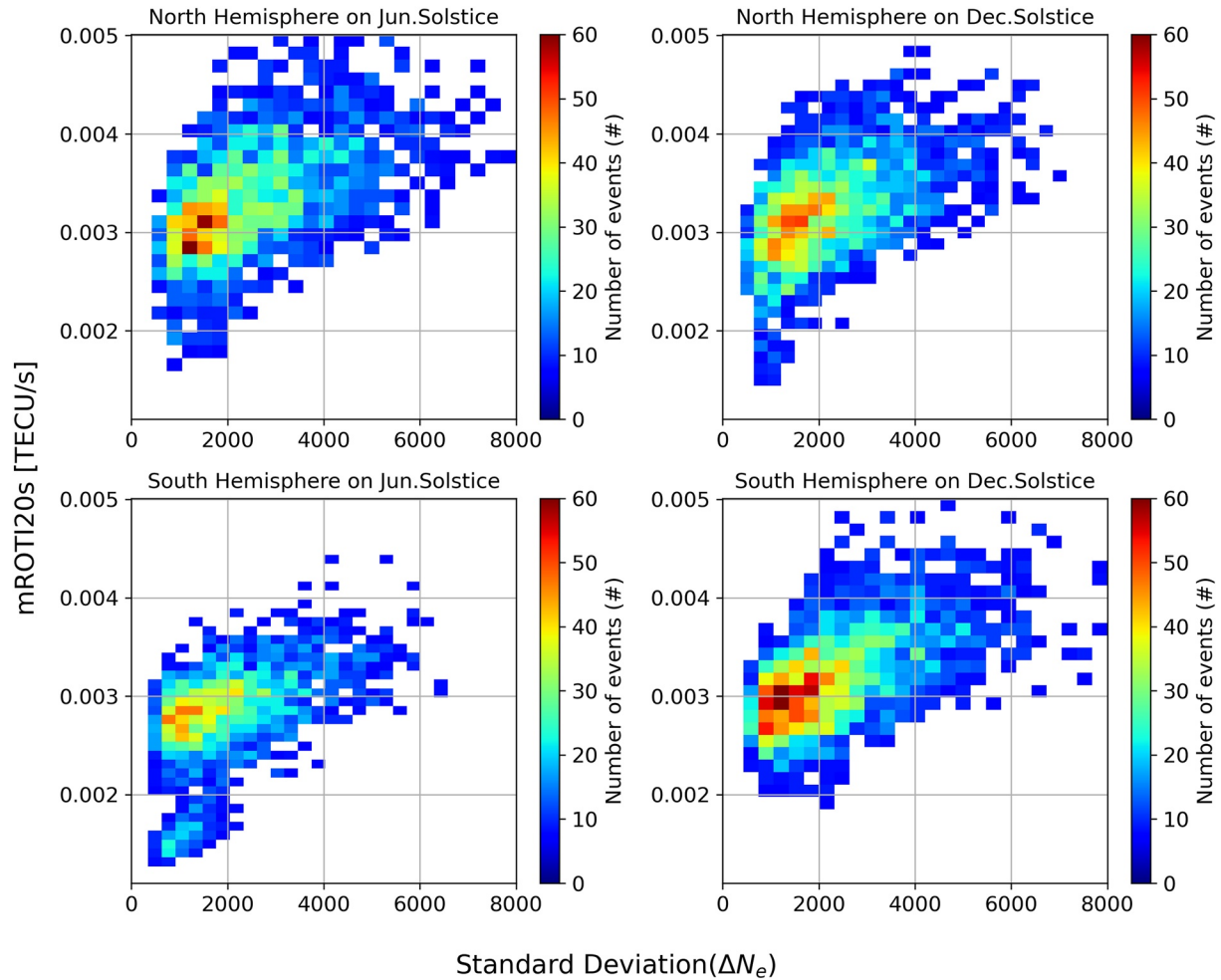


**Figure 5.** Color scatter plots of the standard deviation of electron density perturbation ( $\Delta N_e$ ) and mROTI20s from Swarm-C data. The x-axis represents the standard deviation of the electron density perturbation ( $\Delta N_e$ ), the y-axis is the corresponding ROTI value, and the color bar indicates the number of events. The top row is for the northern hemisphere, and the bottom row is relevant to the southern hemisphere. The left column belongs to the June solstice while the right column represents the December solstice.

and C data (i.e.,  $R_{\max} > 0.5$  and the standard deviation of  $\Delta N_e > 8,000 \text{ cm}^{-3}$ ), are dominated by MSTID. It is because the wavefronts in Figure 4 form backward-C shapes virtually straddling the dip equator, as reported by earlier ground-based observations of MSTIDs (e.g., Otsuka et al., 2004; Shiokawa et al., 2003). In addition, at lower latitudes (e.g.,  $|\text{MLAT}| \sim 30^\circ$ ), the wavefront direction becomes closer to the meridional direction (i.e., south-southwest or north-northeast), and likewise, at higher latitudes (e.g.,  $|\text{MLAT}| \sim 50^\circ$ ), the wavefront direction tends toward the zonal direction (i.e., the west-southwest or east-northeast). The dependence of wavefront directions ( $|\theta_{\text{mag}}|$ ) on  $|\text{MLAT}|$  agrees with previous studies on MSTIDs, such as Yokoyama et al. (2009, and references therein) and Fu et al. (2022, Page 9). To summarize, the hemisphere-dependent wavefront directions (i.e., the backward-C shape) and their dependence on  $|\text{MLAT}|$  all support that the disturbances observed by Swarm in the nighttime mid-latitude ionosphere can be practically identified as MSTIDs.

For completeness, we have checked the dependence of  $|\theta_{\text{mag}}|$  on MLT. Figure 6 is a semicircular histogram similar to Figure 4, but each column corresponds to a different MLT sector, with the early evening located to the left and post-midnight regions to the right. The dependence of wavefront directions on MLT (Figure 6) is not as clear as for  $|\text{MLAT}|$  (Figure 4). For example, the wavefront directions do not change monotonically between 20 MLT and 02 MLT (the three leftmost columns), as can be gleaned from the mean  $\theta_{\text{mag}}$  values below each panel. The complex dependence of wavefront directions on MLT conforms to previous ground-based studies on MSTIDs. The MSTID wavefront directions in existing literature were not well organized by MLT (Chen et al., 2019; Cheng

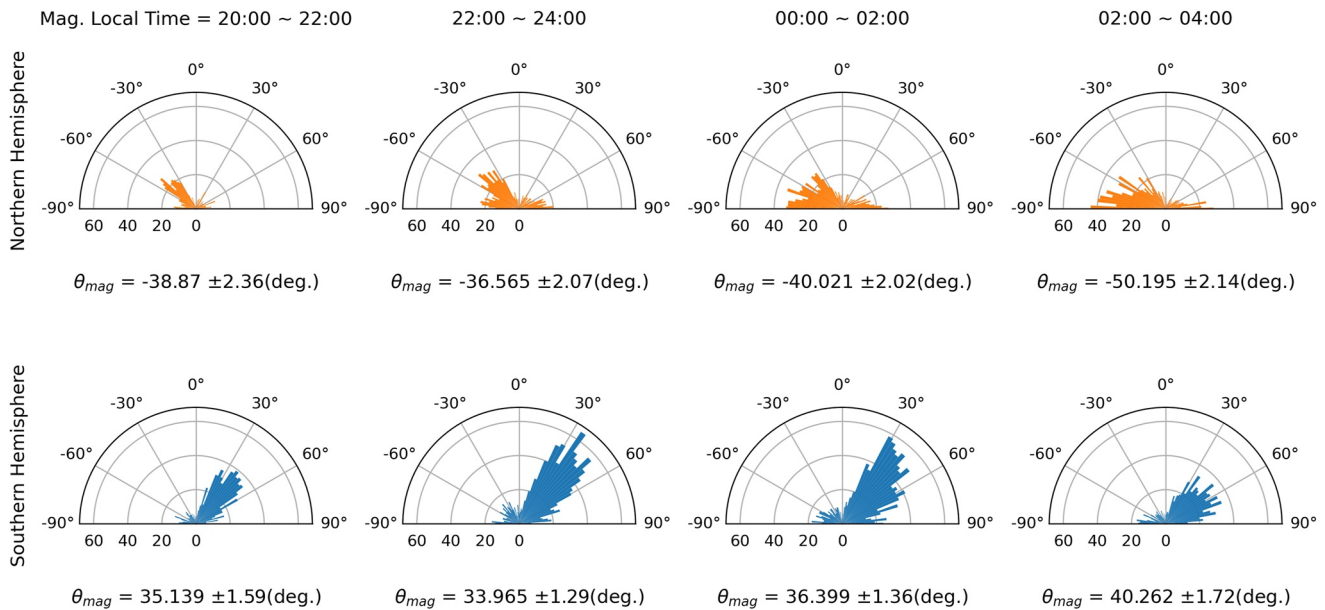


**Figure 6.** Similar to Figure 4, but with each column representing a range of Magnetic Local Time (MLT). The left and right columns correspond to early evening and post-midnight regions, respectively. The orange plots on the top row are for the northern hemisphere, and the blue plots below are for the southern hemisphere.

et al., 2021; He et al., 2004; Oinats et al., 2016; Otsuka et al., 2021) while they are well-aligned with MLAT (Fu et al., 2022; Yokoyama et al., 2009). In summary, the dependence of  $\theta_{mag}$  (or perturbation directivity) on the hemisphere,  $|\text{MLAT}|$ , and MLT strongly supports that the perturbations observed by Swarm at nighttime mid-latitude topside ionosphere can be identified as topside signatures of MSTIDs, at least for strong and coherent events (i.e.,  $R_{max} > 0.5$  and the standard deviation of  $\Delta N_e > 8,000 \text{ cm}^{-3}$ ).

To check the robustness of our results against  $R_{max}$  thresholds, we have redrawn Figures 2, 4, 5, and 6, which were relevant to  $R_{max} > 0.5$ , with a different  $R_{max}$  threshold:  $R_{max} > 0.6$ . The results are Figures S1–S4 in Supporting Information S1. The monotonic  $|\text{MLAT}|$  dependence of  $\theta_{mag}$  in Figure 4 is slightly compromised in the northernmost MLAT bin in Figure S2 in Supporting Information S1 (top right panel; MLAT =  $50^\circ \sim 60^\circ$ ), possibly because only a limited number of events exist there. Except for that, the main features in Figures 2, 4, 5, and 6 remain the same under the change of  $R_{max}$  from 0.5 to 0.6.

We note that the backward-C shape has also been associated with equatorial plasma bubbles (EPBs) by previous studies, such as Kelley et al. (2003), Xiong et al. (2016), and Aa et al. (2020). However, it is generally accepted that the EPBs and MSTIDs are two different phenomena, despite their common backward-C shapes. EPBs usually occur at  $|\text{MLAT}| < 20^\circ$  (e.g., Stolle et al., 2006, Figure 7; Xiong et al., 2010, Figure 9), with the hottest spot in the Brazilian longitude during December solstice (e.g., Stolle et al., 2006, Figure 6). On the contrary, MSTIDs are known to be a mid-latitude phenomenon, which rarely propagates to the equatorward of Appleton Anomaly peaks or  $|\text{MLAT}| \sim 15^\circ$  (e.g., Narayanan et al., 2014). As our study focuses on the region of  $|\text{MLAT}| = 20^\circ \sim 55^\circ$ , and the event distributions (Figure 2) exhibit no (EPB-like) hotspot in the Brazilian longitude during the December solstice, we can assume that our statistics are not severely contaminated by the effects of EPBs.

We note one limitation of our study as described below. Due to the lower-latitude limit imposed by our data processing method ( $\pm 20^\circ$  MLAT), we cannot investigate low-latitude MSTIDs (e.g., equatorward of the Appleton Anomaly peaks) that are sometimes observed at night (e.g., Sivakandan et al., 2021). We are unaware of any method that can clearly distinguish the LEO snapshot of low-latitude MSTIDs from that of EPBs. Hence, we opt to focus our study only on mid-latitudes, and further studies are needed to generalize our results to low-latitude MSTIDs.

As mentioned in Section 2, for every orbit segment we have derived  $R_{max}$  and  $\theta_{mag}$  over  $\pm 6^\circ$  GLAT (in total  $12^\circ$ ) around the selected peak, which roughly occupies a third of the total orbit segment. Hence, one may ask whether our results can truly represent the whole orbit segment: simply speaking, whether fluctuations within the selected

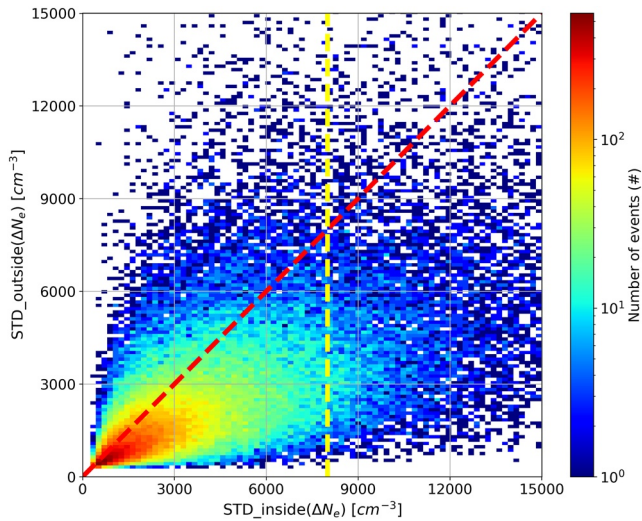


**Figure 7.** Comparison of standard deviations of  $\Delta N_e$  for the data points used for Rmax estimation and those neglected. The x-axis represents the standard deviation of  $\Delta N_e$  used for Rmax estimation, and the y-axis represents the standard deviation of  $\Delta N_e$  for the remaining data points. The red dashed line indicates the perfect agreement between the abscissa and ordinate, and the yellow dashed vertical line represents the detection threshold for intense fluctuation events ( $\Delta N_e > 8,000 \text{ cm}^{-3}$ ), which was used for  $\theta_{\text{mag}}$  calculation. The color palette expresses the number of events (i.e., orbit segments) on a log scale.

third (i.e.,  $\pm 6^\circ$  GLAT) are stronger than for the remaining data points that are neglected during the Rmax estimation. Hence, to check the reliability of the methodology, we compare the standard deviation of  $\Delta N_e$  in the latitude range where the Rmax is estimated (peak  $\pm 6^\circ$  in GLAT) and that in the remaining portion, which was not used in Section 3. Figure 7 is a 2-dimensional graph of all the orbit segments. The x-axis represents the standard deviation of  $\Delta N_e$  for the  $\pm 6^\circ$  latitude used for the Rmax estimation (i.e., the values investigated in Section 3), and the y-axis is the standard deviation of  $\Delta N_e$  in the rest data for each orbit segment (i.e., the portion neglected in Section 3). The red dashed line represents the perfect agreement between the x- and y-axes, and the yellow dashed line displays the  $\Delta N_e = 8,000 \text{ cm}^{-3}$  threshold, which was used as a criterion to find intense fluctuation events in Section 3. The color palette expresses the number of orbit segments (i.e., events) per bin on a log scale. The reddish population near the bottom-left corner corresponds to orbit segments with little to no fluctuations, which is of little interest in this study, while the bluish population near the top-right corner represents strong fluctuations. In Figure 7, the majority of the data points lie below the red dashed line (perfect agreement), which indicates that the standard deviation of  $\Delta N_e$  is larger for the data points used in Section 3 (and in Rmax estimation) than for the neglected portions. This trend is especially clear for the intense ( $\Delta N_e > 8,000 \text{ cm}^{-3}$ ) fluctuation events used for  $\theta_{\text{mag}}$  calculation (e.g., Figure 4), which occupy the region to the right of the yellow dashed line. Among the 10,028 intense ( $\Delta N_e > 8,000 \text{ cm}^{-3}$ ) fluctuation events, 94.296% lie below the red dashed line. Hence, we can conclude that our analysis results in Section 3 represent the dominant part of nightside mid-latitude ionospheric perturbations.

#### 4.2. Other New Findings About Topside MSTIDs

As the Swarm-observed perturbations can be largely identified with MSTIDs (see Section 4.1), we may further deduce the following properties of nighttime MSTIDs using the Swarm data. Figure 3 demonstrated that the plasma density profiles observed by Swarm A and C become less coherent (i.e., Rmax decreases) as the zonal separation of the two spacecraft ( $\Delta \text{GLON}$ ) increases. Because no previous studies have performed such coherence analysis with MSTIDs, this paper provides the first quantitative measure of distance-dependent coherence of MSTID substructures. The decrease of coherence (Rmax) with increasing inter-satellite distance ( $\Delta \text{GLON}$ ) gives firm observational evidence that an MSTID is not such an infinite plane wave (i.e., perfect homogeneity along the wavefront direction) as is commonly assumed in simplified descriptions (e.g., Tsunoda, 2006, Figure 3; Ogawa et al., 2009, Figure 13; Kawai et al., 2021, Figures 10c–10d), but can have inhomogeneous or finite wavefronts. This inhomogeneity or finiteness of MSTID wavefronts was demonstrated earlier in realistic simulation results (e.g., Yokoyama & Hysell, 2010, Figures 3 and 4) or individual 2D images (e.g., Kelley & Makela, 2001, Plate 1), but our Figure 3 gives its statistical proof for the first time.

Another important point in this study is that MSTIDs can even affect the TEC above Swarm A and C (at altitudes of about 470 km). The topside TEC disturbance has been reported previously in case studies (e.g., Lou et al., 2019), but not in statistical analyses to the best of the authors' knowledge. It would be informative to compare the topside TEC fluctuation levels related to MSTIDs (at mid-latitude regions) with those at other latitudes. A study of topside ROTI data of Swarm in high-latitude regions suggested that ROTI has a disturbance magnitude of  $\sim 0.01 \text{ TECU/s}$  (Jin et al., 2019). In low-latitude regions, the ROTI of the Swarm data can frequently increase beyond 5 TECU/s (Zakharenkova et al., 2016, Figures 4 and 5). In Figure 5, mROTI20s values are generally below 0.01 TECU/s, which means that mid-latitude perturbations in this study (or equivalently, MSTIDs) can incur topside TEC variations weaker than equatorial or high-latitude perturbations. The low intensity of MSTID-related topside TEC perturbations is as expected from previous studies using in situ plasma density, such as Jin et al. (2020, Figure 3).

Our analysis method, which is based on cross-correlating Swarm tandem observations, inherits the basic philosophy from previous studies, such as Xiong et al. (2016). The method can also be extended to other LEO spacecraft

fleets consisting of more than two satellites: for example, the Small scale magNetospheric and Ionospheric Plasma Experiment (SNIPE) mission scheduled to be launched in 2023 (Lee et al., 2022; Song et al., 2021). SNIPE is a project to observe the space environment with four 6U cube satellites at 500 km of altitude in a Sun-synchronous orbit (Kim et al., 2022). SNIPE is equipped with the Solid State Telescope (SST; Sohn et al., 2018), Magnetometer (MAG; Song et al., 2021), Langmuir Probe (LP), Gamma Ray burst Monitor (GRM) and Iridium and GPS Board (IGB; Song, Lee, & Yi, 2022). It will conduct tandem observation through formation flight by maintaining the inter-spacecraft distance (Kang et al., 2020). During the first half of the mission lifetime, the four SNIPE satellites will be placed into a pearls-on-a-string configuration, from which we may deduce MSTID velocities, as described in Section 2.

## 5. Conclusions

We analyze the quasi-2D characteristics of perturbations in the nighttime mid-latitude topside ionosphere using tandem observations of in situ plasma density by Swarm A and C satellites. The wavefront direction with respect to the geomagnetic north ( $\theta_{\text{mag}}$ ) is calculated from the latitudinal offset between the observed disturbance profiles ( $\Delta\text{GLAT}$ ) and the zonal distance between the satellites ( $\Delta\text{GLON}$ ). We mainly focus on intense (standard deviation of  $\Delta N_e > 8,000 \text{ cm}^{-3}$ ) and coherent ( $R_{\text{max}}$  between different spacecraft  $> 0.5$ ) events. The main science outputs obtained from this technique can be summarized as follows.

1. [*wavefront direction*] The derived wavefronts conform to backward-C shapes virtually straddling the dip equator. The wavefront directions ( $\theta_{\text{mag}}$ ) are more and more inclined toward the north-south direction as the latitude decreases while the directions do not depend on MLT as clearly. All these features of the wavefront directions ( $n\theta_{\text{mag}}$ ) confirm that MSTIDs are the dominant driver of the nighttime mid-latitude topside perturbations observed by Swarm, at least of the events that imprint intense and coherent features on both Swarm A and C data. As the seasonal/geographical distributions of our events (Figure 2) are consistent with similar previous studies based on 1D in situ measurements, our results also support the assertions made by previous studies (e.g., Kil & Paxton, 2017; Lee et al., 2021; Park et al., 2010) that the 1D perturbations observed in the nighttime mid-latitude topside largely represent MSTIDs.
2. [*ROTI*] Moreover, we demonstrate that the nighttime mid-latitude topside perturbations observed by Swarm (or *topside* MSTIDs) are accompanied by TEC fluctuations above the spacecraft (i.e., ROTI). It indicates that the perturbations encountered by Swarm feature localized electric field, as nighttime MSTIDs have been traditionally considered to host. Note that the disturbance level is lower than for typical equatorial or high-latitude disturbances reported in previous studies.
3. [*finite wavefronts*] Also, we quantitatively showed that the coherence between the plasma density profiles observed by Swarm A and C decreases with the increasing zonal distance between the two spacecraft. It indicates that MSTIDs cannot always be simplified to infinite plane waves, but inhomogeneity or finiteness along the wavefront should be fully considered.

Overall, our results demonstrate that plasma perturbations in the nighttime mid-latitude topside can be identified as MSTID in its traditional definition (e.g., the characteristic wavefront directions and possible connection to the localized electric field), which is the most important finding of this study.

## Data Availability Statement

The  $N_e$ ,  $T_e$ , TEC, and ROTI data of Swarm satellites can be accessed from the official Swarm website of ESA ([https://swarm-diss.eo.esa.int/#swarm%2FLevel2daily%2FLatest\\_baselines%2FIPD%2FIRR](https://swarm-diss.eo.esa.int/#swarm%2FLevel2daily%2FLatest_baselines%2FIPD%2FIRR)), and directory is Home-Level2daily-Latest\_baselines-IPD-IRR data. The post-processed Swarm data used for drawing statistical figures in this paper is given as a CSV file at the following link: <https://doi.org/10.5281/zenodo.7536473>.

## References

- Aa, E., Zou, S., Eastes, R., Karan, D. K., Zhang, S.-R., Erickson, P. J., & Coster, A. J. (2020). Coordinated ground-based and space-based observations of equatorial plasma bubbles. *Journal of Geophysical Research: Space Physics*, 125(1), e2019JA027569. <https://doi.org/10.1029/2019JA027569>
- Altadill, D., Segarra, A., Blanch, E., Juan, J. M., Paznukhov, V. V., Buresova, D., et al. (2020). A method for real-time identification and tracking of traveling ionospheric disturbances using ionosonde data: First results. *Journal of Space Weather and Space Climate*, 10(2013), 2. <https://doi.org/10.1051/swsc/2019042>

## Acknowledgments

This research was supported by the Korea Astronomy and Space Science Institute under the R&D program (Project No. 2023-1-850-10) supervised by the Ministry of Science and ICT. JP was supported by the National Research Council of Science & Technology (NST) grant by the Korean government (MSIT; No. CPS21161-120).



- Buchert, S., Zangerl, F., Sust, M., André, M., Eriksson, A., Wahlund, J., & Opgenoorth, H. (2015). SWARM observations of equatorial electron densities and topside GPS track losses. *Geophysical Research Letters*, 42(7), 2088–2092. <https://doi.org/10.1002/2015GL063121>
- Chen, G., Zhou, C., Liu, Y., Zhao, J., Tang, Q., Wang, X., & Zhao, Z. (2019). A statistical analysis of medium-scale traveling ionospheric disturbances during 2014–2017 using the Hong Kong CORS network. *Earth Planets and Space*, 71(1), 52. <https://doi.org/10.1186/s40623-019-1031-9>
- Cheng, P. H., Lin, C., Otsuka, Y., Liu, H., Rajesh, P. K., Chen, C. H., et al. (2021). Statistical study of medium-scale traveling ionospheric disturbances in low-latitude ionosphere using an automatic algorithm. *Earth Planets and Space*, 73(1), 1–17. <https://doi.org/10.1186/s40623-021-01432-1>
- Crowley, G., Jones, T. B., & Dudeney, J. R. (1987). Comparison of short period TID morphologies in Antarctica during geomagnetically quiet and active intervals. *Journal of Atmospheric and Terrestrial Physics*, 49(11), 1155–1162. [https://doi.org/10.1016/0021-9169\(87\)90098-5](https://doi.org/10.1016/0021-9169(87)90098-5)
- Dinsmore, R., Mathews, J. D., Coster, A., Robinson, R. M., Sarkhel, S., Erickson, P. J., & Urbina, J. (2021). Multi-instrument observations of SCIPS: 1. ISR and GPS TEC results. *Journal of Atmospheric and Solar-Terrestrial Physics*, 213, 105515. <https://doi.org/10.1016/j.jastp.2020.105515>
- Friis-Christensen, E., Lühr, H., Knudsen, D., & Haagmans, R. (2008). Swarm - An Earth observation mission investigating geospace. *Advances in Space Research*, 41(1), 210–216. <https://doi.org/10.1016/j.asr.2006.10.008>
- Frissell, N. A., Baker, J. B. H., Ruohoniemi, J. M., Greenwald, R. A., Gerrard, A. J., Miller, E. S., & West, M. L. (2016). Sources and characteristics of medium-scale traveling ionospheric disturbances observed by high-frequency radars in the North American sector. *Journal of Geophysical Research: Space Physics*, 121(4), 3722–3739. <https://doi.org/10.1002/2015JA022168>
- Frissell, N. A., Kaeppler, S. R., Sanchez, D. F., Perry, G. W., Engelke, W. D., Erickson, P. J., et al. (2022). First observations of large scale traveling ionospheric disturbances using automated amateur radio receiving networks. *Geophysical Research Letters*, 49(5), e2022GL097879. <https://doi.org/10.1029/2022GL097879>
- Fu, W., Yokoyama, T., Ssessanga, N., Yamamoto, M., & Liu, P. (2022). On using a double-thin-shell approach and TEC perturbation component to sound night-time mid-latitude E–F coupling. *Earth Planets and Space*, 74(1), 83. <https://doi.org/10.1186/s40623-022-01639-w>
- Hajkowicz, L. A. (1990). A global study of large scale travelling ionospheric disturbances (TIDS) Following a step-like onset of auroral substorms in both hemispheres. *Planetary and Space Science*, 38(7), 913–923. [https://doi.org/10.1016/0032-0633\(90\)90058-X](https://doi.org/10.1016/0032-0633(90)90058-X)
- Hajkowicz, L. A., & Hunsucker, R. D. (1987). A simultaneous observation of large-scale periodic TIDs in both hemispheres following an onset of auroral disturbances. *Planetary and Space Science*, 35(6), 785–791. [https://doi.org/10.1016/0032-0633\(87\)90038-9](https://doi.org/10.1016/0032-0633(87)90038-9)
- He, L. S., Dyson, P. L., Parkinson, M. L., & Wan, W. (2004). Studies of medium scale travelling ionospheric disturbances using TIGER SuperD-ARN radar sea echo observations. *Annales Geophysicae*, 22(12), 4077–4088. <https://doi.org/10.5194/angeo-22-4077-2004>
- Hernández-Pajares, M., Juan, J. M., Sanz, J., Aragón-Ángel, A., García-Rigo, A., Salazar, D., & Escudero, M. (2011). The ionosphere: Effects, GPS modeling and the benefits for space geodetic techniques. *Journal of Geodesy*, 85(12), 887–907. <https://doi.org/10.1007/s00190-011-0508-5>
- Huang, C.-S., de La Beaujardiere, O., Roddy, P. A., Hunton, D. E., Liu, J. Y., & Chen, S. P. (2014). Occurrence probability and amplitude of equatorial ionospheric irregularities associated with plasma bubbles during low and moderate solar activities (2008–2012). *Journal of Geophysical Research: Space Physics*, 119(2), 1186–1199. <https://doi.org/10.1002/2013JA019212>
- Huang, F., Lei, J., Dou, X., Luan, X., & Zhong, J. (2018). Nighttime medium-scale traveling ionospheric disturbances from airglow imager and Global Navigation Satellite Systems observations. *Geophysical Research Letters*, 45(1), 31–38. <https://doi.org/10.1002/2017GL076408>
- Hunsucker, R. D. (1982). Atmospheric gravity waves generated in the high-latitude ionosphere: A review. *Reviews of Geophysics*, 20(2), 293. <https://doi.org/10.1029/RG020i002p00293>
- Jeong, S. H., Lee, W. K., Jang, S., Kil, H., Kim, J. H., Kwak, Y. S., et al. (2022). Reconstruction of the regional total electron content maps over the Korean Peninsula using deep convolutional generative adversarial network and Poisson blending. *Space Weather*, 20(8), e2022GL097879. <https://doi.org/10.1029/2022SW003131>
- Jin, Y., Kotova, D., Xiong, C., Brask, S. M., Clausen, L. B. N., Kervalishvili, G., et al. (2022). Ionospheric plasma Irregularities - IPIR - data product based on data from the Swarm satellites. *Journal of Geophysical Research: Space Physics*, 127(4), e2021JA030183. <https://doi.org/10.1029/2021JA030183>
- Jin, Y., Spicher, A., Xiong, C., Clausen, L. B. N., Kervalishvili, G., Stolle, C., & Miloch, W. J. (2019). Ionospheric plasma irregularities characterized by the Swarm satellites: Statistics at high latitudes. *Journal of Geophysical Research: Space Physics*, 124(2), 1262–1282. <https://doi.org/10.1029/2018JA026063>
- Jin, Y., Xiong, C., Clausen, L., Spicher, A., Kotova, D., Brask, S., et al. (2020). Ionospheric plasma irregularities based on in situ measurements from the Swarm satellites. *Journal of Geophysical Research: Space Physics*, 124(7), e2020JA028103. <https://doi.org/10.1029/2020JA028103>
- Jonah, O. F., Kherani, E. A., & De Paula, E. R. (2017). Investigations of conjugate MSTIDs over the Brazilian sector during daytime. *Journal of Geophysical Research: Space Physics*, 122(9), 9576–9587. <https://doi.org/10.1002/2017JA024365>
- Kang, S., Song, Y., & Park, S. Y. (2020). Nanosat formation flying design for SNIPE mission. *Journal of Astronomy and Space Sciences*, 37, 51–60. <https://doi.org/10.5140/JASS.2020.37.1.51>
- Kawai, K., Shiokawa, K., Otsuka, Y., Oyama, S., Kasaba, Y., Kasahara, Y., et al. (2021). First simultaneous observation of a night time medium-scale traveling ionospheric disturbance from the ground and a magnetospheric satellite. *Journal of Geophysical Research: Space Physics*, 126(9), e2020JA029086. <https://doi.org/10.1029/2020JA029086>
- Kelley, M. C., & Makela, J. J. (2001). Resolution of the discrepancy between experiment and theory of midlatitude F-region structures. *Geophysical Research Letters*, 28(13), 2589–2592. <https://doi.org/10.1029/2000GL012777>
- Kelley, M. C., Makela, J. J., Paxton, L. J., Kamalabadi, F., Comberiate, J. M., & Kil, H. (2003). The first coordinated ground- and space-based optical observations of equatorial plasma bubbles. *Geophysical Research Letters*, 30, 1766. <https://doi.org/10.1029/2003GL017301>
- Kil, H., & Paxton, L. J. (2017). Global distribution of nighttime medium-scale traveling ionospheric disturbances seen by Swarm satellites. *Geophysical Research Letters*, 44(18), 9176–9182. <https://doi.org/10.1002/2017GL074750>
- Kil, H., Paxton, L. J., Jee, G., & Nikoukar, R. (2019). Plasma blobs associated with medium-scale traveling ionospheric disturbances. *Geophysical Research Letters*, 46(7), 3575–3581. <https://doi.org/10.1029/2019GL082026>
- Kim, H.-D., Choi, W., Kim, M.-K., Kim, J.-H., Kim, K., Kim, J., et al. (2022). Design and development of the SNIPE bus system. *Journal of Space Technology and Applications*, 2(2), 81–103. <https://doi.org/10.52912/jsta.2022.2.2.81>
- Knudsen, D. J., Burchill, J. K., Buchert, S. C., Eriksson, A. I., Gill, R., Wahlund, J. E., et al. (2017). Thermal ion imagers and Langmuir probes in the Swarm electric field instruments. *Journal of Geophysical Research: Space Physics*, 122(2), 2655–2673. <https://doi.org/10.1002/2016JA022571>
- Lee, J., Sohn, J., Park, J., Yang, T. Y., Song, H. S., Hwang, J., et al. (2022). SNIPE mission for space weather research. *Journal of Space Technology and Applications*, 2(2), 104–120. <https://doi.org/10.52912/jsta.2022.2.2.104>
- Lee, W. K., Kil, H., & Paxton, L. J. (2021). Global distribution of nighttime MSTIDs and its association with E region irregularities seen by CHAMP satellite. *Journal of Geophysical Research: Space Physics*, 126(5), e2020JA028836. <https://doi.org/10.1029/2020JA028836>

- Lou, Y., Luo, X., Gu, S., Xiong, C., Song, Q., Chen, B., et al. (2019). Two typical ionospheric irregularities associated with the tropical cyclones Tembin (2012) and Hagibis (2014). *Journal of Geophysical Research: Space Physics*, 124(7), 6237–6252. <https://doi.org/10.1029/2019JA026861>
- Lühr, H., Kervalishvili, G. N., Stolle, C., Rauberg, J., & Michaelis, I. (2019). Average characteristics of low-latitude interhemispheric and F region dynamo currents deduced from the Swarm satellite constellation. *Journal of Geophysical Research: Space Physics*, 124(12), 10631–10644. <https://doi.org/10.1029/2019JA027419>
- MacDougall, J., Abdu, M. A., Batista, I., Fagundes, P. R., Sahai, Y., & Jayachandran, P. T. (2009). On the production of traveling ionospheric disturbances by atmospheric gravity waves. *Journal of Atmospheric and Solar-Terrestrial Physics*, 71(17–18), 2013–2016. <https://doi.org/10.1016/j.jastp.2009.09.006>
- Martinis, C., Baumgardner, J., Mendillo, M., Wroten, J., MacDonald, T., Kosch, M., et al. (2019). First conjugate observations of medium-scale traveling ionospheric disturbances (MSTIDs) in the Europe-Africa longitude sector. *Journal of Geophysical Research: Space Physics*, 124(3), 2213–2222. <https://doi.org/10.1029/2018JA026018>
- Mendillo, M., Baumgardner, J., Nottingham, D., Aarons, J., Reinisch, B., Scali, J., & Kelley, M. (1997). Investigations of thermospheric-ionospheric dynamics with 6300-Å images from the Arecibo Observatory. *Journal of Geophysical Research*, 102(A4), 7331–7343. <https://doi.org/10.1029/96JA02786>
- Narayanan, V. L., Shiokawa, K., Otsuka, Y., & Saito, S. (2014). Airglow observations of nighttime medium-scale traveling ionospheric disturbances from Yonaguni: Statistical characteristics and low-latitude limit. *Journal of Geophysical Research: Space Physics*, 119(11), 9268–9282. <https://doi.org/10.1002/2014JA020368>
- Nematipour, P., Raoofian-Naeni, M., & Ghaffari Razin, M. R. (2022). Regional application of C1 finite element interpolation method in modeling of ionosphere total electron content over Europe. *Advances in Space Research*, 69(3), 1351–1365. <https://doi.org/10.1016/j.asr.2021.11.030>
- Ogawa, T., Igarashi, K., Aikyo, K., & Maeno, H. (1987). NNS satellite observations of medium-scale traveling ionospheric disturbances at southern high-latitudes. *Journal of Geomagnetism and Geoelectricity*, 39(12), 709–721. <https://doi.org/10.5636/jgg.39.709>
- Ogawa, T., Nishitani, N., Otsuka, Y., Shiokawa, K., Tsugawa, T., & Hosokawa, K. (2009). Medium-scale traveling ionospheric disturbances observed with the SuperDARN Hokkaido radar, all-sky imager, and GPS network and their relation to concurrent sporadic E irregularities. *Journal of Geophysical Research*, 114(A3), A03316. <https://doi.org/10.1029/2008JA013893>
- Oinats, A. V., Nishitani, N., Ponomarenko, P., Berngardt, O. I., & Ratovsky, K. G. (2016). Statistical characteristics of medium-scale traveling ionospheric disturbances revealed from the Hokkaido East and Ekaterinburg HF radar data coupling of the high and mid latitude ionosphere and its relation to geospace dynamics. *Earth Planets and Space*, 68(1), 8. <https://doi.org/10.1186/s40623-016-0390-8>
- Onishi, T., Tsugawa, T., Otsuka, Y., Berthelier, J. J., & Lebreton, J. P. (2009). First simultaneous observations of daytime MSTIDs over North America using GPS-TEC and DEMETER satellite data. *Geophysical Research Letters*, 36(11), 1–5. <https://doi.org/10.1029/2009GL038156>
- Otsuka, Y., Onoma, F., Shiokawa, K., Ogawa, T., Yamamoto, M., & Fukao, S. (2007). Simultaneous observations of nighttime medium-scale traveling ionospheric disturbances and E region field-aligned irregularities at midlatitude. *Journal of Geophysical Research*, 112(A6), A06317. <https://doi.org/10.1029/2005JA011548>
- Otsuka, Y., Shinbori, A., Tsugawa, T., & Nishioka, M. (2021). Solar activity dependence of medium-scale traveling ionospheric disturbances using GPS receivers in Japan. *Earth Planets and Space*, 73(1), 22. <https://doi.org/10.1186/s40623-020-01353-5>
- Otsuka, Y., Shiokawa, K., & Ogawa, T. (2012). Disappearance of equatorial plasma bubble after interaction with mid-latitude medium-scale traveling ionospheric disturbance. *Geophysical Research Letters*, 39(14), L14105. <https://doi.org/10.1029/2012GL052286>
- Otsuka, Y., Shiokawa, K., Ogawa, T., & Wilkinson, P. (2004). Geomagnetic conjugate observations of medium-scale traveling ionospheric disturbances at midlatitude using all-sky airglow imagers. *Geophysical Research Letters*, 31(15), L15803. <https://doi.org/10.1029/2004GL020262>
- Otsuka, Y., Suzuki, K., Nakagawa, S., Nishioka, M., Shiokawa, K., & Tsugawa, T. (2013). GPS observations of medium-scale traveling ionospheric disturbances over Europe. *Annales Geophysicae*, 31(2), 163–172. <https://doi.org/10.5194/angeo-31-163-2013>
- Oyama, K. (2015). DC Langmuir probe for measurement of space plasma: A brief review. *Journal of Astronomy and Space Sciences*, 32(3), 167–180. <https://doi.org/10.5140/JASS.2015.32.3.167>
- Park, J. (2022). Coherence scale and directivity of nighttime equatorial plasma irregularities: Results from Swarm formation flight. *Journal of Geophysical Research: Space Physics*, 127(5), e2021JA030233. <https://doi.org/10.1029/2021JA030233>
- Park, J., Lühr, H., Michaelis, I., Stolle, C., Rauberg, J., Buchert, S., et al. (2015). Westward tilt of low-latitude plasma blobs as observed by the Swarm constellation. *Journal of Geophysical Research: Space Physics*, 120(4), 3187–3197. <https://doi.org/10.1002/2014JA020965>
- Park, J., Lühr, H., Min, K. W., & Lee, J. J. (2010). Plasma density undulations in the nighttime mid-latitude F-region as observed by CHAMP, KOMSAT-1, and DMSP F15. *Journal of Atmospheric and Solar-Terrestrial Physics*, 72(2–3), 183–192. <https://doi.org/10.1016/j.jastp.2009.11.007>
- Perwitasari, S., Nakamura, T., Tsugawa, T., Nishioka, M., Tomikawa, Y., Ejiri, M. K., et al. (2022). Propagation direction analyses of medium-scale traveling ionospheric disturbances observed over North America with GPS-TEC perturbation maps by three-dimensional spectral analysis method. *Journal of Geophysical Research: Space Physics*, 127(1), e2020JA028791. <https://doi.org/10.1029/2020JA028791>
- Rajesh, P. K., Liu, J. Y., Lin, C. H., Chen, A. B., Hsu, R. R., Chen, C. H., & Huba, J. D. (2016). Space-based imaging of nighttime medium-scale traveling ionospheric disturbances using FORMOSAT-2/ISUAL 630.0 nm airglow observations. *Journal of Geophysical Research: Space Physics*, 121(5), 4769–4781. <https://doi.org/10.1002/2015JA022334>
- Ryu, K., Lee, J., Kim, S., Chung, T., Shin, G. H., Cha, W., et al. (2017). Characteristics of the plasma source for ground ionosphere simulation surveyed by disk-type Langmuir probe. *Journal of Astronomy and Space Sciences*, 34(4), 343–351. <https://doi.org/10.5140/JASS.2017.34.4.343>
- Saito, A., Fukao, S., & Miyazaki, S. (1998). High resolution mapping of TEC perturbations with the GSI GPS Network over Japan. *Geophysical Research Letters*, 25(16), 3079–3082. <https://doi.org/10.1029/98GL52361>
- Saito, S., Yamamoto, M., & Hashiguchi, H. (2008). Imaging observations of nighttime mid-latitude F-region field-aligned irregularities by an MU radar ultra-multi-channel system. *Annales Geophysicae*, 26(8), 2345–2352. <https://doi.org/10.5194/angeo-26-2345-2008>
- Scharroo, R., & Smith, W. H. F. (2010). A global positioning system - Based climatology for the total electron content in the ionosphere. *Journal of Geophysical Research*, 115(10), A10318. <https://doi.org/10.1029/2009JA014719>
- Shiokawa, K., Otsuka, Y., Ihara, C., Ogawa, T., & Rich, F. J. (2003). Ground and satellite observations of nighttime medium-scale traveling ionospheric disturbance at midlatitude. *Journal of Geophysical Research*, 108, 1145. <https://doi.org/10.1029/2002JA009639>
- Sivakandan, M., Otsuka, Y., Ghosh, P., Shinagawa, H., Shinbori, A., & Miyoshi, Y. (2021). Comparison of seasonal and longitudinal variation of daytime MSTID activity using GPS observation and GAIA simulations. *Earth Planets and Space*, 73(1), 35. <https://doi.org/10.1186/s40623-021-01369-5>
- Smirnov, A., Shprits, Y., Zhelavskaya, I., Lühr, H., Xiong, C., Goss, A., et al. (2021). Intercalibration of the plasma density measurements in Earth's topside ionosphere. *Journal of Geophysical Research: Space Physics*, 126(10), e2021JA029334. <https://doi.org/10.1029/2021JA029334>

- Sohn, J., Lee, J., Jo, G., Lee, J., Hwang, J., Park, J., et al. (2018). Conceptual design of a solid state telescope for small scale magnetospheric ionospheric plasma experiments. *Journal of Astronomy and Space Sciences*, 35, 195–200. <https://doi.org/10.5140/JASS.2018.35.3.195>
- Song, H., Lee, J., & Yi, Y. (2022). Feasibility study of communication access via iridium constellation for small-scale magnetospheric ionospheric plasma experiment mission. *Journal of Astronomy and Space Sciences*, 39(3), 109–116. <https://doi.org/10.5140/JASS.2022.39.3.109>
- Song, H., Park, J., Buchert, S., Jin, Y., Chao, C. K., Lee, J., & Yi, Y. (2022). A small peak in the Swarm-LP plasma density data at the dayside dip equator. *Journal of Geophysical Research: Space Physics*, 127(7), e2022JA030319. <https://doi.org/10.1029/2022JA030319>
- Song, H., Park, J., & Lee, J. (2021). Magnetometer calibration based on the CHAOS-7 model. *Journal of Astronomy and Space Sciences*, 38(3), 157–164. <https://doi.org/10.5140/JASS.2021.38.3.157>
- Song, Q., Ding, F., Wan, W., Ning, B., Liu, L., Zhao, B., et al. (2013). Statistical study of large-scale traveling ionospheric disturbances generated by the solar terminator over China. *Journal of Geophysical Research: Space Physics*, 118(7), 4583–4593. <https://doi.org/10.1002/jgra.50423>
- Stolle, C., Lühr, H., Rother, M., & Balasis, G. (2006). Magnetic signatures of equatorial spread F as observed by the CHAMP satellite. *Journal of Geophysical Research*, 111(A2), A02304. <https://doi.org/10.1029/2005JA011184>
- Su, S. Y., Liu, C. H., Ho, H. H., & Chao, C. K. (2006). Distribution characteristics of topside ionospheric density irregularities: Equatorial versus midlatitude regions. *Journal of Geophysical Research*, 111(6), A06305. <https://doi.org/10.1029/2005JA011330>
- Tsugawa, T., Otsuka, Y., Coster, A. J., & Saito, A. (2007). Medium-scale traveling ionospheric disturbances detected with dense and wide TEC maps over North America. *Geophysical Research Letters*, 34(22), L22101. <https://doi.org/10.1029/2007GL031663>
- Tsunoda, R. T. (2006). On the coupling of layer instabilities in the nighttime midlatitude ionosphere. *Journal of Geophysical Research*, 111(A11), A11304. <https://doi.org/10.1029/2006JA011630>
- Xiong, C., Park, J., Lühr, H., Stolle, C., & Ma, S. Y. (2010). Comparing plasma bubble occurrence rates at CHAMP and GRACE altitudes during high and low solar activity. *Annales Geophysicae*, 28(9), 1647–1658. <https://doi.org/10.5194/angeo-28-1647-2010>
- Xiong, C., Stolle, C., Lühr, H., Park, J., Fejer, B. G., & Kervalishvili, G. N. (2016). Scale analysis of equatorial plasma irregularities derived from Swarm constellation. *Earth Planets and Space*, 68(1), 121. <https://doi.org/10.1186/s40623-016-0502-5>
- Yadav, V., Rath, R., Gaur, G., Sarkhel, S., Chakrabarty, D., Sunil Krishna, M. V., et al. (2021). Interaction between nighttime MSTID and mid-latitude field-aligned plasma depletion structure over the transition region of geomagnetic low-mid latitude: First results from Hanle, India. *Journal of Atmospheric and Solar-Terrestrial Physics*, 217, 105589. <https://doi.org/10.1016/j.jastp.2021.105589>
- Yang, H., Monte-Moreno, E., Hernández-Pajares, M., & Roma-Dollase, D. (2021). Real-time interpolation of global ionospheric maps by means of sparse representation. *Journal of Geodesy*, 95(6), 1–20. <https://doi.org/10.1007/s00190-021-01525-5>
- Yin, F., Lühr, H., Park, J., & Wang, L. (2019). Comprehensive analysis of the magnetic signatures of small-scale traveling ionospheric disturbances, as observed by Swarm. *Journal of Geophysical Research: Space Physics*, 124(12), 10794–10815. <https://doi.org/10.1029/2019JA027523>
- Yokoyama, T., & Hysell, D. L. (2010). A new midlatitude ionosphere electrodynamics coupling model (MIECO): Latitudinal dependence and propagation of medium-scale traveling ionospheric disturbances. *Geophysical Research Letters*, 37(8), L08105. <https://doi.org/10.1029/2010GL042598>
- Yokoyama, T., Hysell, D. L., Otsuka, Y., & Yamamoto, M. (2009). Three-dimensional simulation of the coupled Perkins and Es-layer instabilities in the nighttime midlatitude ionosphere. *Journal of Geophysical Research*, 114(A3), A03308. <https://doi.org/10.1029/2008JA013789>
- Zakharenkova, I., Astafyeva, E., & Cherniak, I. (2016). GPS and in situ Swarm observations of the equatorial plasma density irregularities in the topside ionosphere. *Earth Planets and Space*, 68(1), 120. <https://doi.org/10.1186/s40623-016-0490-5>
- Zakharenkova, I., Cherniak, I., & Kravtsov, A. (2019). Features of storm-induced ionospheric irregularities from ground-based and spaceborne GPS observations during the 2015 St. Patrick's Day Storm. *Journal of Geophysical Research: Space Physics*, 124(12), 10728–10748. <https://doi.org/10.1029/2019JA026782>
- Zhang, S.-R., Erickson, P. J., Gasque, L. C., Aa, E., Rideout, W., Vierinen, J., et al. (2021). Electrified postsunrise ionospheric perturbations at Millstone Hill. *Geophysical Research Letters*, 48(18), e2021GL095151. <https://doi.org/10.1029/2021GL095151>